Biomass derived porous carbon for superior electrocatalysts for oxygen reduction reaction

Chunyu Zhu, [a,b *] *Bo Zhao,* [a] *Manami Takata,* [b] *Yoshitaka Aoki,* [b] *Hiroki Habazaki* [b]

[a] School of Low-carbon Energy and Power Engineering, China University of Mining and Technology, Xuzhou, 221116, China

[b] Faculty of Engineering, Hokkaido University, Sapporo 060-8628, Japan.

Corresponding Author

* E-mail: zcyls@cumt.edu.cn

ABSTRACT

The preparation of porous carbon from biomass flour as high-performance electrocatalysts for oxygen reduction reaction (ORR) was reported in this paper. The fast and vigorous pyrolysis of flour was induced in the presence of magnesium nitrate, by which MgO nanoparticles were introduced as nano-template to create numerous nanopores and to increase the specific surface area (SSA). The pore structure, SSA and elemental dopant were influenced by the ratio of biomass to magnesium nitrate and calcination temperature. A highly hierarchical micro-meso-macroporous carbon, which was calcined at 1000 ^{o}C and had a high SSA of 1880 m^2 g^{-1}, exhibited the best ORR performance in terms of fast ORR kinetic, superior stability and excellent methanol tolerance.

KEYWORDS oxygen reduction reaction, porous carbon, electrocatalysts, biomass

1. Introduction

The development of clean and efficient electrochemical energy conversion devices, for example the fuel cells and metal-air batteries, has drawn great attentions because of their environmental friendliness and high energy density. However, the sluggish kinetics for oxygen reduction reaction (ORR) in the cathode side has hindered the large-scale practical application. Towards this end, a lot of efficient ORR electrocatalysts have been explored. Although platinum (Pt) and its alloys have been widely investigated and been proved to be the most effective electrocatalysts for ORR, the scarcity, expensiveness and bad tolerance to CO poisoning and methanol crossover have impeded their widespread application [1, 2]. Recently, carbon materials have been widely investigated as the substitute to Pt, because of their good electric conductivity, low price and abundance in nature. The electrocatalytic ORR properties of carbon can be greatly accelerated by heteroatom-doping, such as N, S and P etc [3-6]. So far, most of the doped carbon electrocatalysts are manufactured by the high-temperature pyrolysis process, for example, by the direct pyrolytic formation of carbon accompanying with the addition of heteroatom-comprising resources and the secondary doping treatment of carbon precursors with heteroatom-comprising chemicals [7-10]. However, most of the heteroatom doped carbon electrocatalysts are fabricated using fossil oil derived chemicals, which inevitably increases the cost of the catalysts. Therefore, it is very attractive to fabricate carbon electrocatalysts by a facile and efficient process using cheap, naturally abundant and renewable biomass-derived raw materials. Additionally, biomass precursors often contain required C and N, making them good resources for producing heteroatom-doped carbon [11, 12]. Recently, biomass-derived carbon electrocatalysts with good electrochemical performance have been reported by several groups, such as using sengon

wood [13], lotus root [14], ginkgo leaves [15], catkin [16], sawdust [17], spinach leaves [18], biomass waste [19]. Despite these successes in developing biomass carbons, it still seems difficult to achieve highly efficient carbon electrocatalysts with large specific surface area (SSA) and optimized pore architecture. Herein, we present a simple preparation process for porous biomass carbon by pyrolyzing flour in the presence of magnesium nitrate, which can enhance the efficient pyrolysis of biomass precursor and introduce MgO nanoparticles as template to create numerous nanopores and to increase the specific surface area. The relationship between pore architecture, SSA of the biomass carbons and their ORR electrocatalytic properties is carefully studied.

2. Experiment

Preparation of porous carbon:

Commercial flour powders (see Table S1 for the composition analysis) with weights of 0.7, 0.85 and 1.0 g were gelatinized in distilled water at 80 ºC respectively, after which magnesium nitrate hexahydrate ($Mg(NO_3)_2 \cdot 6H_2O$, 2.564 g) was added. The mixtures were stirred while the water was evaporated, and finally dried gels were obtained. The dried gels were undergone a preliminary decomposition process by being heated to 500 ºC under Ar atmosphere for 1 h, after which the samples were carbonized at 900, 1000 or 1200 ºC for 2 h. These samples were then dispersed in 0.5 mol L^{-1} HCl to dissolve the soluble materials, which were filtrated, washed by distilled water and ethanol for several times. Finally, the samples were dried. Five samples were obtained, which were named based on the flour amount and carbonization temperature, i.e., S0.7-1000, S0.85-1000, S1.0-1000, S0.85-900 and S0.85-1200.

Material characterization:

The samples were characterized by X-ray diffraction (XRD, Rigaku Miniflex, CuKα), scanning transmission electron microscopy (STEM, JEOL, JEM-ARF-200) and scanning electron microscopy (SEM, JEOL, JSM-7400F) for their crystallite phase composition and microstructure analysis. A RENISHAW Raman spectrometer was employed to get the Raman spectra of carbon samples. The X-ray photoelectron spectroscopy (XPS) analysis was carried out on an X-ray photoelectron spectrometer (JEOL, JPS-9200). The SSA, pore volume and pore size distribution of the specimens were investigated by N_2 absorption measurement using a BELSORP-mini equipment (Bel Japan).

Electrochemical measurement:

The rotating disk electrode (RDE) system was employed to measure the electrocatalytic ORR properties, which was connected to a Princeton electrochemical analyzer [20]. As for the counter electrode a Pt sheet was employed, while as the reference electrode the Ag/AgCl electrode saturated with KCl solution electrolyte was used. The working electrodes were glassy carbon (GC) electrodes coated with the as-prepared electrocatalysts. The GC has a diameter of 5 mm. 2.0 mg catalyst powders were dispersed in a solution containing 400 μL ethanol and 20 μL 5% Nafion solution, which was subsequently ultrasonically agitated for 30 min to prepare the catalyst ink. The polished GC electrode was coated with 3, 6, 10 or 15 μL catalyst ink, corresponding to mass load of around 73, 146, 243 and 364 μg cm^{-2}. The electrolyte was 0.1 M KOH. The potential values in this work have been converted to the reversible hydrogen electrode (RHE). In every measurement, the electrolyte was firstly saturated with Ar or O_2 gas for 30 min. In the case of RDE tests, the linear sweep voltammetry (LSV) measurement for ORR was conducted under a series of rotation speeds from 400 to 1600 rpm, and the scan rate is 10

mV s^{-1}. The cyclic voltammetry (CV) curves were obtained at a scan rate of 50 mV s^{-1} in both Ar and O_2 saturated electrolyte. The electron transfer number (n) was analyzed by using the Koutecky–Levich (K-L) method.

The chronoamperometric I–t curves were obtained at -0.4 V vs. Ag/AgCl. The electrochemical active surface area (ECSA) of the electrocatalysts were estimated by comparing the double layer capacitance (C_{dl}) values with that of GC electrode surface (0.2 F m^{-2}) [21]. The C_{dl} was estimated from CV curves in a non-faradic potential range of 0.21 to 0.26 V vs Ag/AgCl.

3. Results and Discussion

3.1 Morphology and structural analysis of the porous carbon

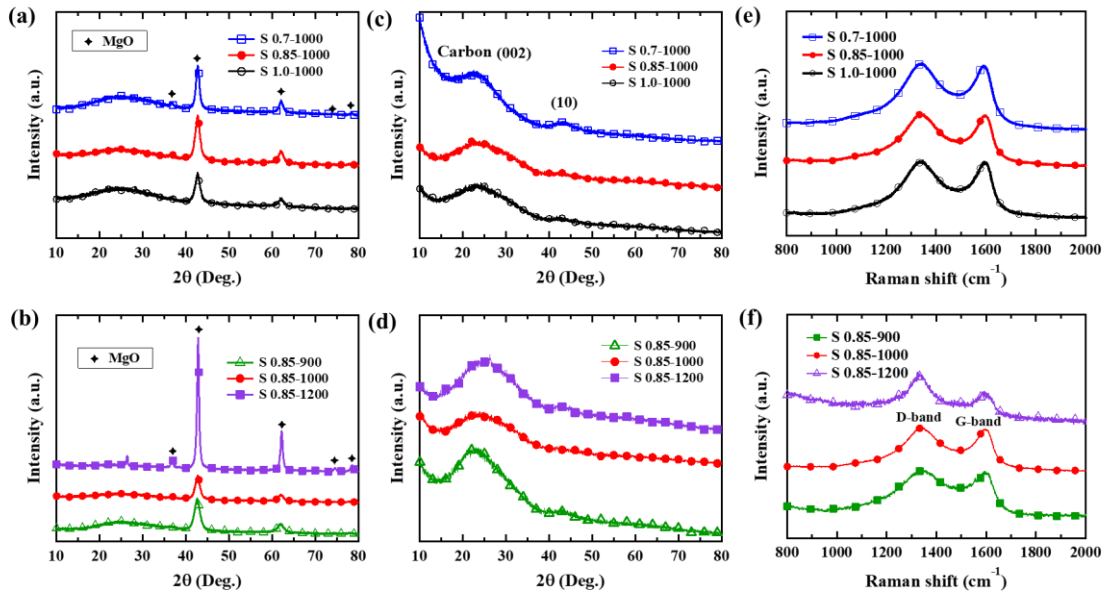

Fig. 1 XRD patterns and Raman spectra of the samples. (a, b) XRD patterns of the calcined samples; (c, d) XRD pattern and (e, f) Raman spectra of the carbon samples obtained after washing

The porous carbon samples were prepared by using biomass flour as carbon source. Magnesium nitrate was gelatinized with flour in hot water to make a homogenous mixture. After decomposition and carbonization, the flour-derived carbon was embedded with MgO nanoparticles, which were good templates for creating numerous nanopores and could be easily removed by washing with acid solution.

The XRD patterns of the specimens obtained after heat treatment and washing treatment are shown in Fig. 1a-d. The samples after heat treatment (a, b) present obvious peaks corresponding to the MgO phase (JCPDS No: 00-004-0829), together with broad peaks near 24 º referring to carbon. After washing treatment with HCl solution, the peaks of MgO disappear and the samples (c, d) show the typical patterns of amorphous carbon which has broad peaks at 24 and 42 º. The characteristics of the samples were further characterized by Raman spectroscopy, as shown in Fig. 1e-f. The Raman spectra present two dominant peaks at ~ 1350 and 1585 cm^{-1}, referring to the disordered D-band and graphitic G-band of carbon, respectively. The intensity ratio of I_D/I_G is normally used to evaluate the disorder degree of carbon. The values of I_D/I_G ratios based on area for these samples are calculated to be larger than 1, illustrating the low graphitization characteristic of the samples. As for the samples treated at 900, 1000 and 1200 °C, the intensity ratio is decreased from 3.13, 3.05 to 2.70 respectively, demonstrating the enhanced graphitization degree as the increase of carbonization temperature.

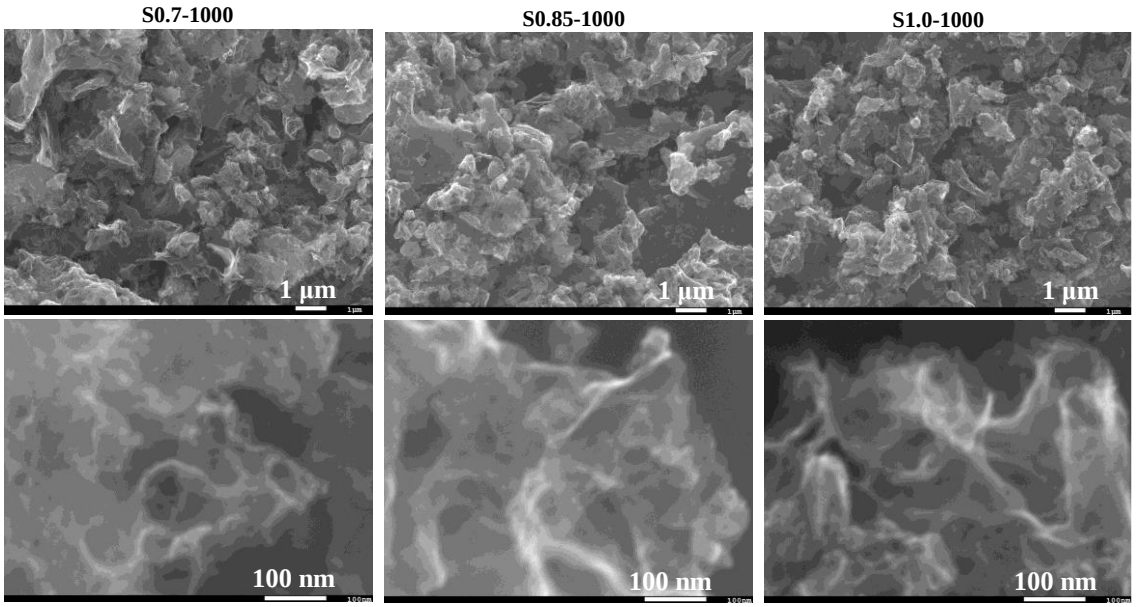

Fig. 2 SEM images of the samples obtained after washing treatment

Fig. 2 and Fig. 3 present the typical SEM and TEM/STEM images of the carbon samples. These morphology observations illustrate that the carbon products have a three-dimensionally hierarchical porous structure, which is constructed with abundant opened pores in multi scales from micropores (< 2 nm) to mesopores (2 ~ 50 nm) and macropore (> 50 nm). The high-resolution TEM image as shown in Fig. 3b indicates that the carbon sample is highly disordered and amorphous. From the highly magnified STEM image in Fig. 3d, it is observed that there are many highly dispersed atomic metallic sites (the white dots). These atoms could be the metallic residues such as Fe and Cu deriving from the biomass flour. It is well known that these metallic atoms are good catalytic sites for enhancing the ORR performance [22, 23].

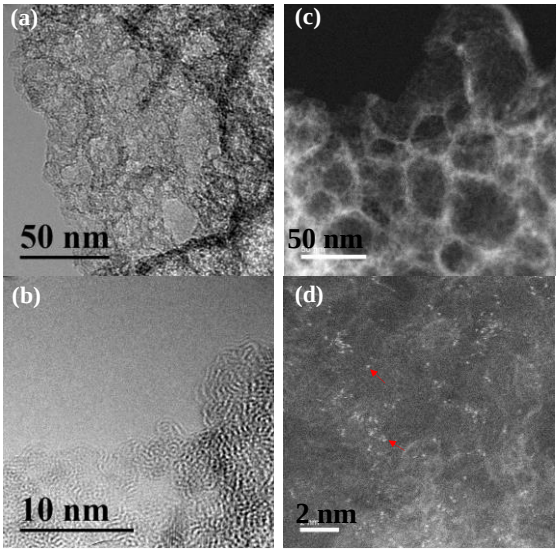

Fig. 3 TEM (a, b) and STEM (c, d) images of carbon sample S0.85-1000

The porous structural characteristics of the specimens were further analyzed by N_2 absorption experiment. Fig. 4 exhibits the N_2 absorption isotherms and pore size distribution for the samples both after heat treatment and after washing treatment. The samples exhibit the type IV isotherms, which have hysteresis loops at relative pressure of around 0.5-0.9. This indicates the presence of a lot of mesopores. In a N_2 absorption isotherm, a strong adsorption at the relative pressure near 0 represents the existence of micropores, while a steep adsorption near 1.0 indicates the existing of macropores. For the calcined samples before HCl washing, the isotherms present steep absorption near 1.0, but limited nitrogen absorption near 0. This indicates that those samples contain a lot of macropores, but very few micropores. After acid washing treatment, the isotherms of the final carbon products (excluding S0.7-1000) present steep absorption both near 0 and 1.0, indicating the coexisting of a lot of micropore and macropores. The pore characteristics were further confirmed by their pore size distributions, which were analyzed by non-localized density functional theory (NLDFT) method. The samples (Fig. 4b,d) obtained

after heat treatment present a small amount of micropores and a large amount of mesopore and macropores. The samples (Fig. 4b,d) obtained after acid washing present greatly increased amount of pores from micropores to mesopores and macropores, excluding sample S0.7-1000 which mainly contains micropores and mesopores with sizes less than 7 nm.

The pore formation mechanism is shown as below: 1) During the decomposition process of flour and magnesium nitrate, a lot of mesopores and macropores were created due to ejection of pyrolysis gases. 2) After heat treatment, highly porous composites containing porous carbon matrix and embedded MgO nanoparticles were prepared, and subsequently after acid washing, the MgO nano-templates was dissolved, which induced the formation a lot of micropores and small mesopores. 3) As for sample S0.7-1000, since that lower amount of carbon source was used, MgO particles occupied as the main part of the composite, and after acid washing to remove MgO, the originally large pore structure containing large mesopores and macropores collapsed. The porous structure characteristics for the samples are summarized in Table 1.

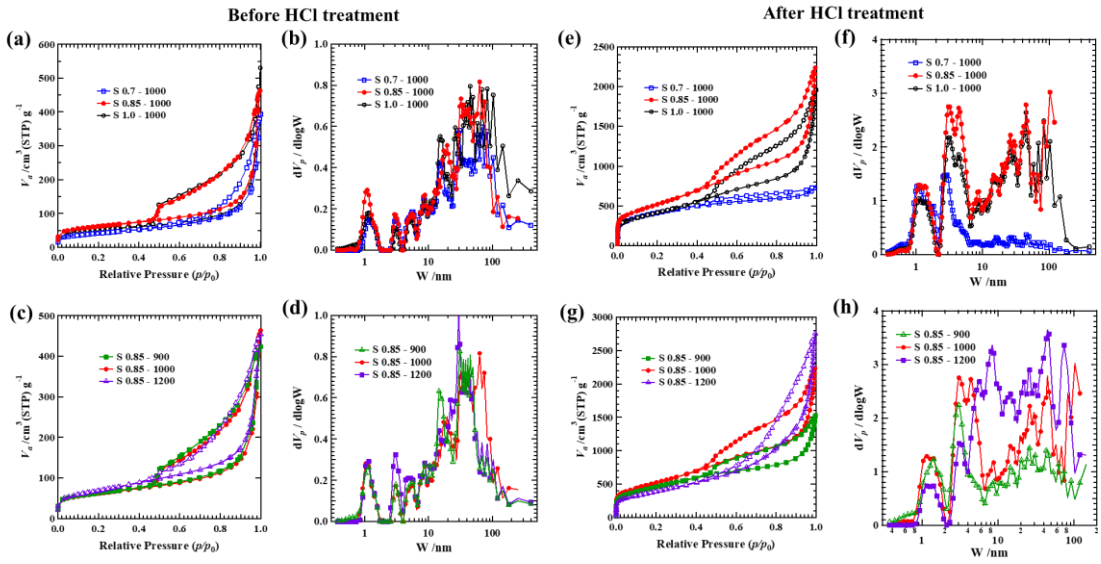

Fig. 4 Nitrogen absorption analysis of the samples. (a, c, e, g) Nitrogen absorption isotherm; (b, d, f, h) NLDFT pore size distribution

Table 1. Porous structure properties of the samples as-characterized by N_2 absorption.

Samples	BET SSA	a_{total}	a_{ex}	a_{micro} = a_{total}-a_{ex}	$V_{0.99}$	$V_{0.95}$	V_{micro}	V_{meso} = $V_{0.95}$-V_{micro}
	[m^2 g^{-1}]	[m^2 g^{-1}]	[m^2 g^{-1}]	[m^2 g^{-1}]	[cm^3 g^{-1}]	[cm^3 g^{-1}]	[cm^3 g^{-1}]	[cm^3 g^{-1}]
Samples obtained after heat treatment (composites of carbon and MgO)								
S0.7 - 1000	145	-	-	-	0.5	0.3	-	-
S0.85 - 900	222	-	-	-	0.6	0.3	-	-
S0.85 - 1000	218	-	-	-	0.6	0.3	-	-
S0.85 - 1200	242	-	-	-	0.6	0.4	-	-
S1.0 - 1000	181	-	-	-	0.6	0.3	-	-
Final porous carbon obtained after acid washing								
S0.7 - 1000	1490	1451	117	1334	1.1	1.0	0.8	0.2
S0.85 - 900	1645	1535	370	1165	2.2	1.6	0.9	0.7
S0.85 - 1000	1880	1794	533	1261	3.2	2.2	1.2	1.0
S0.85 - 1200	1411	1356	877	479	4.1	2.7	1.0	1.7
S1.0 - 1000	1493	1467	582	885	2.8	1.9	0.8	1.1

BET SSA: specific surface area as-calculated from the adsorption data by Brunauer-Emmett-Teller (BET) method; $V_{0.99}$: total pore volume at P/P_0=0.99, corresponding to the pores with diameters up to around 200 nm; $V_{0.95}$: total pore volume at P/P_0=0.95, corresponding to the pores with diameters up to around 40 nm; a_{total}: the total surface area as-determined by the t-plot method; a_{ex}: the external surface area as-determined by t-plot method; a_{micro}: the micropore surface area as-determined by a_{total}-a_{ex}; V_{micro}: the micropore volume as-analyzed by *t* method; V_{meso}: the mesopore volume as-determined by $V_{0.95}$-V_{micro}. The evaluation of the SSA of the composite samples after heat treatment by t-plot method is not applicable since that those samples do not contain micropores.

Fig. S1 shows the chemical composition and bonding properties of porous carbons as-evaluated by XPS. The widely scanned survey XPS spectra for the samples obtained at different calcination temperatures (Fig. S1a) present three peaks at 285.1, 399.3 and 534.2 eV. These peaks are referred to C 1 s, N 1 s and O 1s, respectively. The intensity ratio of N 1s decreases with the calcination temperature, presenting nitrogen dopant amount of 2.5 atom%, 1.9 atom% and 0.8 atom% for S0.85-900, S0.85-1000 and S0.85-1200, respectively.

3.2 Electrochemical properties as ORR electrocatalyst

The electrocatalytic performance of the porous carbon was investigated using RDE method in 0.1 M KOH electrolyte. Fig. 5a,b show the CV curves of the electrodes in both Ar and O_2-saturated electrolyte. All electrodes exhibit obvious reduction peaks near 0.7-0.8 V vs RHE in O_2-saturated electrolyte, however no evident response in Ar-saturated electrolyte is observed, indicating the electrocatalytic ability to reduce O_2 [24]. The LSV measurements were conducted to examine the ORR kinetics of the carbon electrocatalysts. LSV curves for the electrodes with 6 μL catalyst ink load are compared in Fig. 5c,d. The onset potentials are similar for all electrodes with values of around 0.93 V, excluding that sample S0.85-1200 indicates a value of 0.90 V. The diffusion limiting current densities of the electrodes are quite different. At the same carbonization temperature of 1000 ºC (Fig. 5c), sample S0.85-1000 shows the highest current density, while sample S0.7-1000 presents the lowest. The difference of ORR performance for those samples mainly comes from the porous structure and SSA of carbons. Sample S1.0-1000 and S0.85-1000 have very similar pore structure, which contains hierarchically micro-meso-macropores. However, the SSA of S0.85-1000 (1880 m^2 g^{-1}) is large than S1.0-1000 (1493 m^2 g^{-1}). The sample with a higher SSA possesses more active sites for ORR, thereby inducing a higher diffusion limiting current density for S0.85-1000. The pore structure for sample S0.7-1000 is quite different, containing only micropores and small mesopores that are less than 7 nm. Although the SSA of S0.7-1000 and S1.0-1000 is similar, the current density is increasing slower for S0.7-1000 in the voltage range of 1.0-0.2 V, although the diffusion limiting current density is also identical until 0.1 V. Sample S1.0-1000 has a higher electrocatalytic kinetics than S0.7-1000, in which the highly hierarchical micro-

meso-macropores for S1.0-1000 is beneficial for the efficient mass transfer of the ORR related species including O_2 and OH^- etc. The real ECSA of those samples were measured, which have values of 155, 307 and 286 $m^2\ g^{-1}$ for S0.7-1000, S0.85-1000 and S1.0-1000 respectively, indicating a positive correlation with their ORR performance. See Fig. S2 for the determination of ECSA. This also indicate that the open and hierarchical porous structure is good for offering more accessible active sites.

Fig. 5d compared the LSV curves of the samples obtained at different carbonization temperatures. Sample S0.85-1000 shows the highest current density, while sample S0.85-1200 presents the lowest. The decreased ORR activity for the sample obtained at 1200 ºC is due to the very high carbonization temperature which could remove the N dopant, although the graphitization degree of carbon is increased as confirmed by previous Raman and XPS analysis.

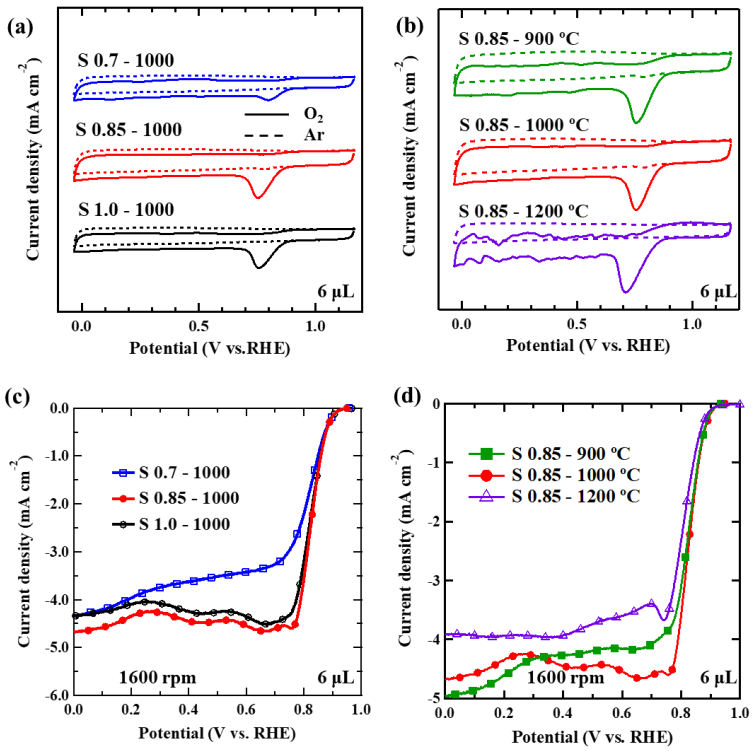

Fig. 5 Electrochemical properties of the carbon catalysts towards oxygen reduction. (a, b)

the CV curves in both Ar and O_2-saturated electrolyte; (c, d) the LSV curves for the electrodes with mass loading of 6 μL at a rotation speed of 1600 rpm

Mass load of catalysts is an important parameter to influence the ORR kinetics. The LSV curves and CV curves obtained at different rotation speeds and different mass load are shown in Fig. S3. Fig. 6 presents the LSV curves of the samples with different mass load (3, 6, 10 and 15 μL catalyst ink) at a rotation speed of 1600 rpm. It is noted that with the increase of catalyst amount, the current density also exhibits an increasing tendency. Higher catalyst amount results in larger surface area and more reaction active sites for the catalyst electrode, thereby presenting higher diffusion-limited current. The increase of current density could reach the maximum for S0.85-1000 and S1.0-1000 at 10 μL, in which the LSV curves almost overlap at 10 and 15 μL. In contrast, S0.7-1000 still present increasing current density by increasing the catalyst load from 10 μL to 15 μL. The SSA and particle size of S0.7-1000 are smaller than those of S0.85-1000 and S1.0-1000. It is difficult for S0.7-1000 to form a uniform catalyst layer on the GC surface because the small carbon particles aggregate easily, especially at a low mass load. Differently, samples S0.85-1000 and S1.0-1000 have larger SSA, micro-meso-macro hierarchical pore structure and lower volume density, the catalyst inks are quite thick and the catalyst layers are uniform on glassy carbon, which is good for the efficient utilization of active sites, presenting much higher ORR activity. With the increase of catalyst load amount, the ORR activity is accelerated. However, the ORR LSV curves for S0.85-1000 and S1.0-1000 at 10 μL and 15 μL still achieve almost the same limiting current plateau. This illustrates that when the surface of the GC electrode is completely covered by the electrocatalyst, catalyst load amount does not influence the diffusion-limited current value.

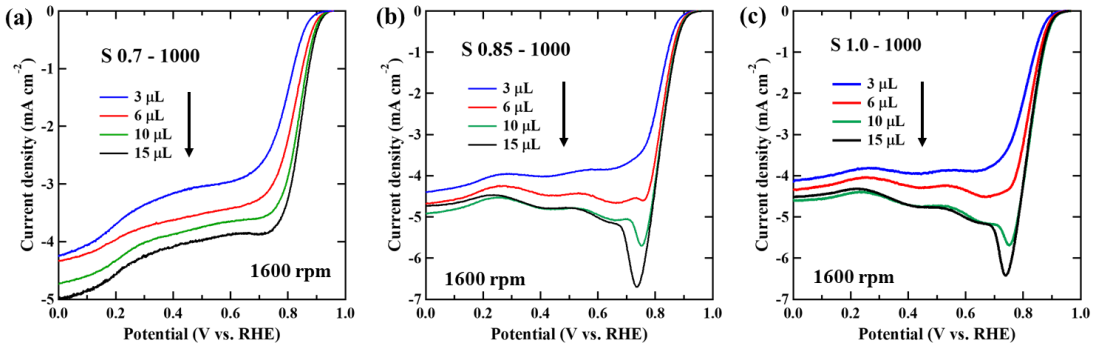

Fig. 6 LSV curves for the electrodes with different mass loading at a rotation speed of 1600 rpm

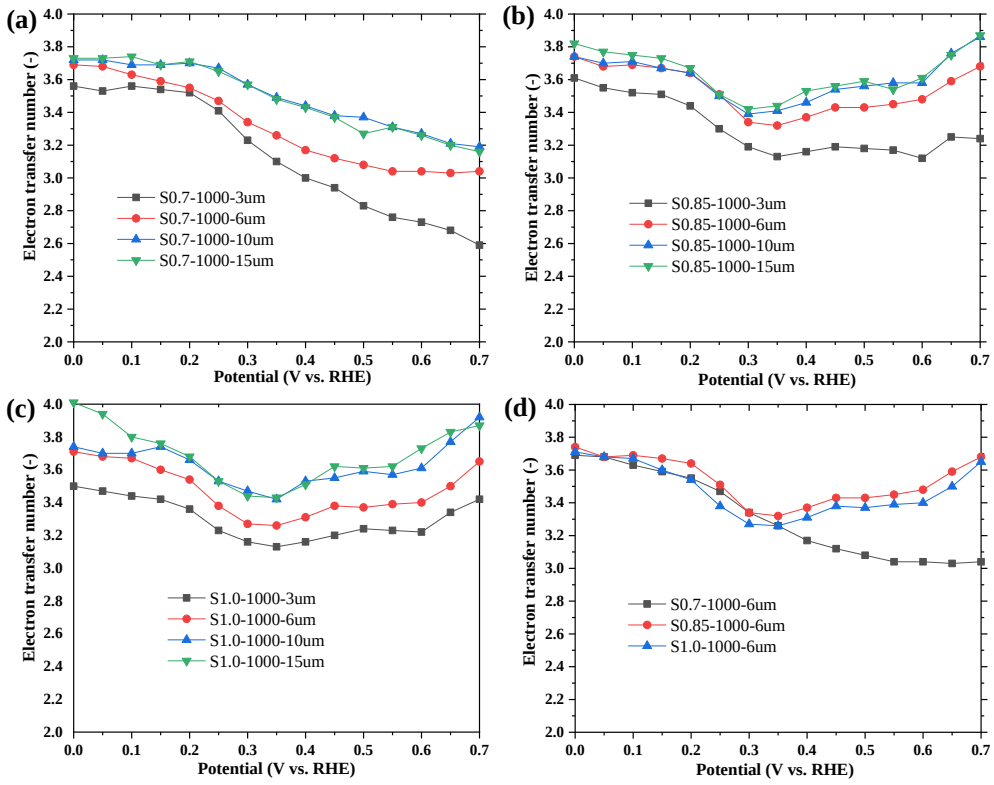

Fig. 7 Electron transfer number n vs. applied potential for the electrodes measured with different mass load. Inset of (d) shows the current density vs. potential from the LSV curves

The electron transfer number *n* of ORR is evaluated by the conventional K-L plot method. The K-L plots are summarized in Fig. S4, which show good linear fitting. The *n*

is calculated and plotted against applied potential, which is presented in Fig. 7. The n values are quite affected by the catalyst load amount and the applied potential. With the increase of catalyst load amount (Fig. 7-a,b,c), the electron transfer numbers increase and approach 4, which reach maximum values at 10 μL. The same phenomenon has been found by other researchers.[25] The n values show fluctuation against applied potential and the fluctuation tendency depends on the porous structure of the carbon catalysts. As compared in Fig. 7-d, the trends of n vs. potential for samples S0.85-1000 and S1.0-1000, which have similar micro-meso-macro hierarchical pore structure, are similar. For these two samples, n has the maximum values at 0.7 V, which decreases until 0.3 V and increases until 0 V. The hierarchically high porous structure is good for the quick ascent of current density at a higher n value. The decreasing of n and the current density from 0.7 V to 0.3 V is due to the exhaustion of oxygen at a higher ORR kinetics. In contrast, for sample S0.7-1000 with narrow micro-meso pores, n has the minimum value at 0.7 V and increases slowly with applied potential, which almost overlap with the n values of another two samples from 0.3 V to 0 V.

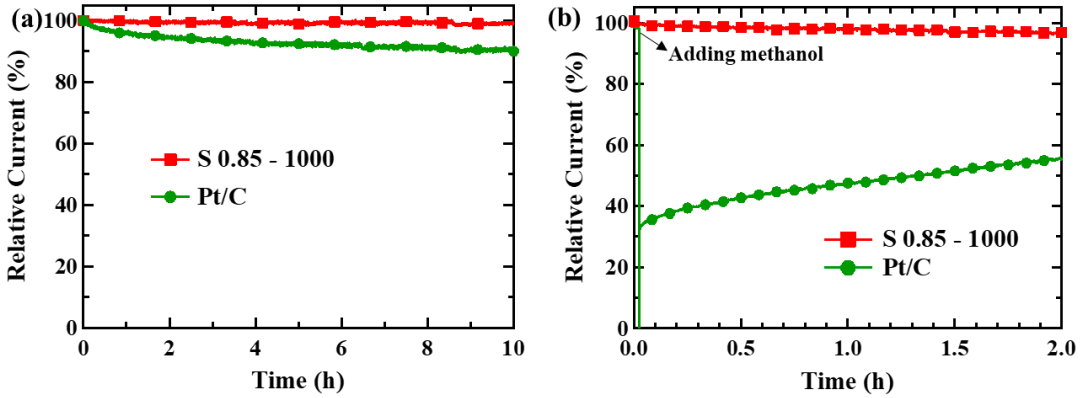

Fig. 8 (a) Chronoamperometric current-time (I-t) curves of S0.85-1000 and Pt/C catalyst in O_2-saturated KOH solution and (b) chronoamperometric I-t curves upon the introduction of methanol

Chronoamperometric measurement was carried out to evaluate the stability of the carbon catalyst. The measurement was conducted under a rotating rate of 1600 rpm at a potential of -0.4 V vs. Ag/AgCl in the aqueous electrolyte of O_2-saturated KOH. As presented in Fig. 8-a, after 10 h, the Pt/C catalyst shows ~10% loss compared with its original current density, while S0.85-1000 has a much better stability which can retain about 99% performance. The carbon catalyst also exhibits good methanol crossover tolerance, as plotted in Fig. 8-b. No obvious change of current was observed during the chronoamperometric measurement by adding 2 vol.% methanol for S0.85-1000, in contrast, the ORR current degraded soon after addition of methanol for Pt/C catalyst. This is due to the occurrence of the methanol oxidation reaction on Pt/C. The carbon catalyst has a strong tolerance against the methanol crossover, making it a promising candidate for alkaline direct methanol fuel cells.

4. Conclusion

In this study, porous carbon for efficient ORR electrocatalyst was prepared from biomass flour. The pyrolysis of flour was assisted by the co-existence of magnesium nitrate, which boosted a fast and vigorous pyrolysis and introduced MgO nanoparticles as template to create numerous nanopores and to enhance the specific surface area. The pore structure of carbon was influenced by the ratio of biomass and magnesium nitrate, by which the hierarchically micro-meso-macroporous carbon and narrowed micro-mesoporous carbon were prepared. The ORR activity was greatly influenced by the pore structure, and the carbon sample with micro-meso-macroporous structure exhibited the best performance. At an optimal calcination temperature of 1000 ^{o}C and an optimal ratio

of flour/magnesium nitrate, the highly hierarchical porous carbon S0.85-1000 exhibited the best ORR performance, including high ORR kinetic, superior stability and good methanol tolerance.

Acknowledgments

This work was partially supported by Natural Science Foundation of Jiangsu Province (No. BK20200635), National Natural Science Foundation of China (No. 52006238). A part of the characterization work was conducted at Hokkaido University, supported by the "Nanotechnology Platform" Program of the Ministry of Education, Culture, Sports, Science and Technology (MEXT), Japan.

References

[1] X.M. Ge, A. Sumboja, D. Wuu, T. An, B. Li, F.W.T. Goh, T.S.A. Hor, Y. Zong, Z.L. Liu,(2015) Oxygen Reduction in Alkaline Media: From Mechanisms to Recent Advances of Catalysts, Acs Catalysis, 5 4643-4667.http://dx.doi.org/10.1021/acscatal.5b00524

[2] M. Tahir, L. Pan, F. Idrees, X.W. Zhang, L. Wang, J.J. Zou, Z.L. Wang,(2017) Electrocatalytic oxygen evolution reaction for energy conversion and storage: A comprehensive review, Nano Energy, 37 136-157.http://dx.doi.org/10.1016/j.nanoen.2017.05.022

[3] C. Hu, L. Dai,(2017) Multifunctional Carbon-Based Metal-Free Electrocatalysts for Simultaneous Oxygen Reduction, Oxygen Evolution, and Hydrogen Evolution, Advanced Materials, 29 1604942-n/a.http://dx.doi.org/10.1002/adma.201604942

[4] Y.-N. Zhu, C.-Y. Cao, W.-J. Jiang, S.-L. Yang, J.-S. Hu, W.-G. Song, L.-J. Wan,(2016) Nitrogen, phosphorus and sulfur co-doped ultrathin carbon nanosheets as a metal-free catalyst for selective oxidation of aromatic alkanes and the oxygen reduction reaction, Journal of Materials Chemistry A, 4 18470-18477.http://dx.doi.org/10.1039/C6TA08335H

[5] J. Guo, S. Zhang, M. Zheng, J. Tang, L. Liu, J. Chen, X. Wang,(2020) Graphitic-N-rich N-doped graphene as a high performance catalyst for oxygen reduction reaction in alkaline solution, International Journal of Hydrogen Energy, 45 32402-32412.http://dx.doi.org/https://doi.org/10.1016/j.ijhydene.2020.08.210

[6] X.L. Qin, Y. Huang, Z.C. Qin, M. Zhao,(2019) Template-free synthesis of novel hollow carbon nanospheres with dual active sites as catalyst for fuel cell cathode to improve oxygen reduction reaction performances, International Journal of Energy Research, 43 8370-8384.http://dx.doi.org/10.1002/er.4833

[7] C. You, X. Jiang, L. Han, X. Wang, Q. Lin, Y. Hua, C. Wang, X. Liu, S. Liao,(2017) Uniform nitrogen and sulphur co-doped hollow carbon nanospheres as efficient metal-free electrocatalysts for oxygen reduction, Journal of Materials Chemistry A, 5 1742-1748.http://dx.doi.org/10.1039/C6TA08674H

[8] K. Wan, A.-d. Tan, Z.-p. Yu, Z.-x. Liang, J.-h. Piao, P. Tsiakaras,(2017) 2D nitrogen-doped hierarchically porous carbon: Key role of low dimensional structure in favoring electrocatalysis and mass transfer for oxygen reduction reaction, Applied Catalysis B: Environmental, 209 447-454.http://dx.doi.org/https://doi.org/10.1016/j.apcatb.2017.03.014

[9] P.K. Sonkar, K. Prakash, M. Yadav, V. Ganesan, M. Sankar, R. Gupta, D.K. Yadav,(2017) Co(ii)-porphyrin-decorated carbon nanotubes as catalysts for oxygen reduction reactions: an approach for fuel cell improvement, Journal of Materials Chemistry A, 5 6263-6276.http://dx.doi.org/10.1039/C6TA10482G

[10] L. Yang, N. Huang, C. Luo, H. Yu, P. Sun, X. Lv, X. Sun,(2021) Atomically dispersed and nanoscaled Co species embedded in micro-/mesoporous carbon nanosheet/nanotube architecture with enhanced oxygen reduction and evolution bifunction for Zn-Air batteries, Chemical Engineering Journal, 404 127112.http://dx.doi.org/https://doi.org/10.1016/j.cej.2020.127112

[11] P. Kaur, G. Verma, S.S. Sekhon,(2019) Biomass derived hierarchical porous carbon materials as oxygen reduction reaction electrocatalysts in fuel cells, Progress in Materials Science, 102 1-71.http://dx.doi.org/https://doi.org/10.1016/j.pmatsci.2018.12.002

[12] W. Yang, S.W. Chen,(2020) Biomass-Derived Carbon for Electrode Fabrication in Microbial Fuel Cells: A Review, Industrial & Engineering Chemistry Research, 59 6391-6404.http://dx.doi.org/10.1021/acs.iecr.0c00041

[13] W. Sudarsono, W.Y. Wong, K.S. Loh, E.H. Majlan, N. Syarif, K.Y. Kok, R.M. Yunus, K.L. Lim,(2020) Noble-free oxygen reduction reaction catalyst supported on Sengon wood (Paraserianthes falcataria L.) derived reduced graphene oxide for fuel cell application, International Journal of Energy Research, 44 1761-1774.http://dx.doi.org/10.1002/er.5015

[14] R. Rajendiran, M. Nallal, K.H. Park, O.L. Li, H.-J. Kim, K. Prabakar,(2019) Mechanochemical assisted synthesis of heteroatoms inherited highly porous carbon from biomass for electrochemical capacitor and oxygen reduction reaction electrocatalysis, Electrochimica Acta, 317 1-9.http://dx.doi.org/https://doi.org/10.1016/j.electacta.2019.05.139

[15] F. Pan, Z. Cao, Q. Zhao, H. Liang, J. Zhang,(2014) Nitrogen-doped porous carbon nanosheets made from biomass as highly active electrocatalyst for oxygen reduction reaction, Journal of Power Sources, 272 8-15.http://dx.doi.org/https://doi.org/10.1016/j.jpowsour.2014.07.180

[16] L. Song, J. Chang, Y. Ma, W. Jiang, Y. Xu, C. Liang, Z. Chen, Y. Zhang,(2020) Biomass-derived nitrogen and sulfur co-doped carbon microtubes for the oxygen reduction reaction, Materials Chemistry Frontiers.http://dx.doi.org/10.1039/D0QM00423E

[17] Y.-Y. Ye, T.-T. Qian, H. Jiang,(2020) Co-Loaded N-Doped Biochar as a High-Performance Oxygen Reduction Reaction Electrocatalyst by Combined Pyrolysis of Biomass, Industrial & Engineering

Chemistry Research, 59 15614-15623.http://dx.doi.org/10.1021/acs.iecr.0c03104
[18] N.-b. Huang, J.-j. Zhang, Y. Sun, X.-n. Sun, Z.-y. Qiu, X.-w. Ge,(2020) A non-traditional biomass-derived N, P, and S ternary self-doped 3D multichannel carbon ORR electrocatalyst, New Journal of Chemistry, 44 14604-14614.http://dx.doi.org/10.1039/D0NJ03283B
[19] S. Xia, W. Guo, N. Cai, L. Sun, H. Zhou, W. Lu, X. Chen, J. Zhang, Y. Chen, H. Yang, F. Sun, D. Wang, X. Wang, S. Wang, H. Chen,(2021) Synthesis and application in oxygen reduction reaction of N-doping porous graphitic carbon from biomass waste, Fuel Processing Technology, 224 107028.http://dx.doi.org/https://doi.org/10.1016/j.fuproc.2021.107028
[20] C. Zhu, M. Takata, Y. Aoki, H. Habazaki,(2018) Nitrogen-doped porous carbon as-mediated by a facile solution combustion synthesis for supercapacitor and oxygen reduction electrocatalyst, Chemical Engineering Journal, 350 278-289.http://dx.doi.org/https://doi.org/10.1016/j.cej.2018.06.001
[21] Y. Cheng, Y. Wang, Q. Wang, Z. Liao, N. Zhang, Y. Guo, Z. Xiang,(2019) Hierarchically porous metal-free carbon with record high mass activity for oxygen reduction and Zn-air batteries, Journal of Materials Chemistry A, 7 9831-9836.http://dx.doi.org/10.1039/C9TA02220A
[22] S.S.A. Shah, T. Najam, M.S. Bashir, M.S. Javed, A.U. Rahman, R. Luque, S.J. Bao,(2022) Identification of Catalytic Active Sites for Durable Proton Exchange Membrane Fuel Cell: Catalytic Degradation and Poisoning Perspectives, Small, 18.http://dx.doi.org/10.1002/smll.202106279
[23] Z.Y. Xiao, P.P. Sun, Z.L. Qiao, K.W. Qiao, H.X. Xu, S.T. Wang, D.P. Cao,(2022) Atomically dispersed Fe-Cu dual-site catalysts synergistically boosting oxygen reduction for hydrogen fuel cells, Chemical Engineering Journal, 446.http://dx.doi.org/10.1016/j.cej.2022.137112
[24] C.Y. Zhu, M. Takata, Y. Aoki, H. Habazaki,(2018) Nitrogen-doped porous carbon as-mediated by a facile solution combustion synthesis for supercapacitor and oxygen reduction electrocatalyst, Chemical Engineering Journal, 350 278-289.http://dx.doi.org/10.1016/j.cej.2018.06.001
[25] G. Zhang, Q. Wei, X. Yang, A.C. Tavares, S. Sun,(2017) RRDE experiments on noble-metal and noble-metal-free catalysts: Impact of loading on the activity and selectivity of oxygen reduction reaction in alkaline solution, Applied Catalysis B: Environmental, 206 115-126.http://dx.doi.org/https://doi.org/10.1016/j.apcatb.2017.01.001